X-RAY FLUORESCENCE MEASUREMENTS OF SKIN IRON CONCENTRATION USING AN ^{125}I-BASED SYSTEM

X-RAY FLUORESCENCE MEASUREMENTS OF SKIN IRON CONCENTRATION USING AN ^{125}I-BASED SYSTEM

By BOBBY TANG, B. Sc

A Thesis Submitted to the Radiation Sciences Graduate Program and School of Graduate Studies

in Partial Fulfillment of the Requirements for the Degree of Masters of Science

McMaster University
MASTER OF SCIENCE (2023)

Hamilton, Ontario
(Radiation Sciences)

TITLE:	X-RAY FLUORESCENCE MEASUREMENTS
	OF SKIN IRON CONCENTRATION USING AN
	^{125}I-BASED SYSTEM
AUTHOR:	Bobby Tang, B.Sc (McMaster University)
SUPERVISORS:	Dr. Michael J. Farquharson
	Dr. Fiona E. McNeill
COMMITTEE:	Dr. Soo Hyun Byun
NUMBER OF PAGES:	xii, 47

Lay Abstract

Iron overload is a prevalent issue in healthcare, with many individuals experiencing detrimental symptoms, such as organ damage and heart failure. Modern treatment significantly improves quality of life but must be continuously monitored.

This thesis covers the development of a non-invasive, cost-effective, and accurate system that can measure skin iron levels in patients to ensure effective monitoring.

The results from this thesis suggest that the system can be used for clinical use to measure patient skin iron levels. It can theoretically measure iron in patients with normal and elevated iron levels. Simulation work suggests that the system will lead to negligible risk from radiation exposure.

While this thesis and its findings support the feasibility of the system, further work is required before clinical implementation of the device.

Abstract

Iron overload conditions are a prevalent issue in global healthcare that require the accurate monitoring of iron levels to effectively provide treatment. X-ray fluorescence has emerged as a candidate for a point-of-care measurement tool for the detection of trace elements *in vivo*. This study explores the feasibility of a portable *in vivo* x-ray fluorescence (IVXRF) instrument using ^{125}I as a point-of-care device in measuring skin iron levels.

The system was calibrated using iron-doped water phantoms for various physiologically-applicable iron concentrations. Measurements were conducted on *ex vivo* rat skin samples ($n = 34$), which were then compared to a benchmark laboratory-based XRF system. Monte Carlo modelling using MCNP 6.2 was used to simulate the system in different conditions and provide an estimate of the radiation dose of the system on soft tissue.

The R^2 value for the calibration line of iron concentration in ppm to normalized iron signal was determined to be 0.985 ($p < 0.01$). For a measurement period of 1800 s real-time, the minimum detectable limit (MDL) of the system is 3.86 ± 0.06 ppm of iron. The R^2 value for the linear regression between the IVXRF and benchmark XRF system normalized iron signals was 0.731 ($p < 0.01$). The R^2 value for the linear regression between the IVXRF normalized iron signal and sample injected iron dose was 0.719 ($p < 0.01$), meaning the system can distinguish between different iron levels in rat skin. From the Monte Carlo simulations, the expected effective dose contribution from the IVXRF system is 101.68 ± 0.03 nSv.

The IVXRF system was shown to accurately measure iron concentrations in *ex vivo* rat skin samples within the iron concentration ranges found within healthy and iron-overloaded patients. Further work shall be conducted to validate the system in *in vivo* applications.

Acknowledgements

I want to thank my supervisors Dr. Michael Farquharson and Dr. Fiona McNeill. Fiona, thank you for your wisdom and guidance these past two years. Mic, being in your group for the past four years has been an absolute pleasure. I have grown in so many ways, both as a researcher and as a person,

Dr. Soo Hyun Byun, thank you for your guidance over the past four years. You always push me to be the best I can be, and I've learned much about the field and how to approach adversity.

Sami, thank you for taking me under your wing these past two years. Your guidance has allowed me to flourish in so many ways. Laura, thank you for always keeping me company in the office these past two years and for helping guide me through.

To all the members of the Sheridan Bruins Men's Volleyball Team, thank you for your unconditional support. Throughout this experience, you taught me the meaning of pursuing what you love and what it means to be a leader. To Kevin, thank you for taking a chance on me and putting me on an unforgettable journey.

To my dear Crystal, thank you for all the love and support you have given me. You always keep me grounded through everything and enable me to be the best version of myself, day in and day out.

Lastly, I would like to thank my parents for always supporting me. You both worked hard to do everything for me, and you instilled the attitude of hard work that is the foundation of my life now.

Table of Contents

Acronyms

XRF: X-ray fluorescence

IVXRF: *In vivo* x-ray fluorescence

SDD: Silicon drift detector

MDL: Minimum detectable limit

MCNP: Monte Carlo N-type Particle Transport code

EGS: Electron Gamma Shower

GEANT: GEometry ANd Tracking

ICRP: International Commission on Radiological Protection

AAPM: American Association of Physicists in Medicine

List of Figures

Declaration of Academic Achievement

I declare that all the work covered in this thesis is my own doing and that I am the sole author of this thesis.

I have read through the thesis and ensured that all of the content is my creation.

Preface

The following thesis has areas of overlap between the material discussed in the paper. Chapter 1 and the Introduction section of the paper overlap when discussing iron overload conditions and means of treatment. Chapter 3 and the Methods section of the paper overlap when discussing the experimental setups. Chapter 4 and the Methods section of the paper overlap when discussing the simulations constructed using Monte Carlo. Chapter 5 and the Discussions section of the paper overlap when discussing the limitations of the study and future avenues of work.

Chapter 1

1 Introduction

1.1 Iron overload conditions

Iron overload conditions are a prevalent issue in global health, with conditions such as β-thalassemia and hereditary hemochromatosis affecting a significant proportion of the worldwide population. [1, 2, 3] Within a healthy individual, iron in the blood is transported around the body through the protein transferrin, which facilitates the safe transport of blood iron. [4] Iron overload arises from the buildup of excess iron in the blood, where transferrin is saturated, and the excess iron exceeds its capacity to transport iron. This overload can then lead to the formation of free radical iron. [5]

If not properly treated, iron overload conditions can lead to iron buildup in organs such as the heart and liver. [6] With the buildup of iron in organs also comes the risk of organ damage, such as through cirrhosis. Iron buildup in the heart can also lead to dysfunction of the heart, which in turn can lead to heart failure through restrictive cardiomyopathy and diastolic dysfunction. [5, 7]

1.1.1 Thalassemia major

β-thalassemias are a group of conditions where red blood cell hemoglobin production is inhibited due to a mutation in the beta-globin (HBB) gene, which leads to ineffective erythropoiesis. [8] This reduced capacity of red blood cells leads to anemia and other symptoms such as growth deficiencies, poor musculature, jaundice, and osteoporosis. [1] To improve the quality of life of thalassemic patients, patients can undergo blood transfusions to maintain a healthy hemoglobin count. [9] However, if not properly monitored, these transfusions can lead to iron overload, which can lead to

symptoms such as diabetes and growth retardation. [10] Some conditions classified as β-thalassemias include thalassemia major, thalassemia intermedia, hemoglobin E thalassemia, and hemoglobin H disease, with the most severe, thalassemia major, requiring blood transfusions as a part of treatment.

1.1.2 Hereditary Hematochromatosis

Similar to thalassemia major, hereditary hemochromatosis is a condition that can lead to the occurrence of iron overload disease. The condition occurs most commonly amongst people from northern Europe, with an incidence of 5 per 1000 people. [3] Hemochromatosis occurs in response to a genetic mutation that affects *HFE* expression. The HFE gene controls hepcidin expression in the body, a protein that controls intestinal iron absorption. When the HFE gene is mutated, hepcidin production is reduced, leading to the unregulated uptake of iron in the intestines. [11] Symptoms from hemochromatosis include diabetes, hypothyroidism, osteoporosis, cirrhosis, and lethargy. [11]

1.1.3 Treatments of iron overload

One of the primary treatments for β-thalassemias is iron chelation therapy, which allows the body to excrete excess iron. [12] The idea behind chelation is that a chelating agent, e.g. deferoxamine (DFO), promotes the formation of complexes with iron, which the body can then excrete. Chelation therapy and blood transfusions allow thalassemic patients to have sufficient blood levels for healthy growth and development while preventing iron overload. Chelation has also been shown to improve cardiac functionality by reducing cardiac burden. [7] The primary treatment for hereditary hemochromatosis is phlebotomy, or removing blood to lower iron levels, with iron chelation being an alternative form of therapy. [3, 13]

While chelation therapy has been shown to be effective in treating iron overload, patient iron levels must be monitored to quantify chelator efficiency. Liver biopsies are considered the gold standard of iron levels and are often used to diagnose hereditary hemochromatosis, but they are

invasive and can lead to surgical complications. [6, 13] Magnetic resonance imaging (MRI) has also been shown to be accurate in measuring iron levels, along with superconducting quantum interface devices (SQUIDs); however, they are expensive to maintain, and MRI techniques are continuing to be further optimized. [14, 15] One of the most common monitoring methods is measuring patient blood serum ferritin levels; however, they can be unreliable due to ferritin levels tending to increase with inflammation. [16] In addition, while patient blood serum ferritin levels can be performed in a day, they take longer to process than the duration of a patient appointment. Physicians must make follow-up telephone appointments with patients to discuss the results, which can add an extra time burden on both the patient and the physician. There is a need for an accurate, quick, cost-effective, and non-invasive point-of-care device for monitoring patient iron levels.

1.2   X-ray fluorescence

X-ray fluorescence (XRF) is a phenomenon that occurs after an atom undergoes photo-absorption or the excitation of electrons in response to an incident photon. [17] Given a target atom, incoming particles can excite electrons into photo-electrons, which lead to the emission of x-rays by the target atom. These x-rays are characteristic of the target element, which allows them to be effective in measuring quantities of specific elements.

The photoelectric effect, or the excitation of an electron into an ejected photoelectron, is an essential interaction in the production of x-ray fluorescence. The probability of the photoelectric effect τ depends on the incident particle's energy E, as well as the atomic number of the target atom Z. Equation 1 shows a rough estimate of this probability, with n being in the range of 4 to 5. [18]

$$\tau \approx constant \times \frac{Z^n}{E^{3.5}} \tag{1}$$

From this energy dependence in correlation to other photon interactions such as Compton scat-

tering and pair production, photoelectric effect interactions tend to be prominent in low energy

ranges ($>$ 100 keV). In comparison, Compton scattering dominates in the energy range of $0.1 - 2$

MeV, and pair production is prominent for high energy ranges ($>$ 10 MeV).

The basis of measuring trace elements through XRF revolves around the photoelectric effect

and the subsequent emission of characteristic x-rays, or x-rays with energies distinct to the target

atom. [17] If incident radiation has enough energy to ionize an electron, that orbital electron would

be emitted with an energy equal to the difference between the incident radiation and the binding

energy of the ejected photo-electron. Once the photo-electron is ejected, a vacancy is formed, which is

subsequently filled by another orbital electron fluorescing from a higher orbital shell. The fluorescing

electron would then emit an x-ray with an energy equal to the difference between the electron's initial

binding energy and its final binding energy. The electron shells that orbit a nucleus are designated

as K-shell (n = 1), L-shell (n = 2), M-shell (n = 3), N-shell (n = 4) and O-shell (n = 5).
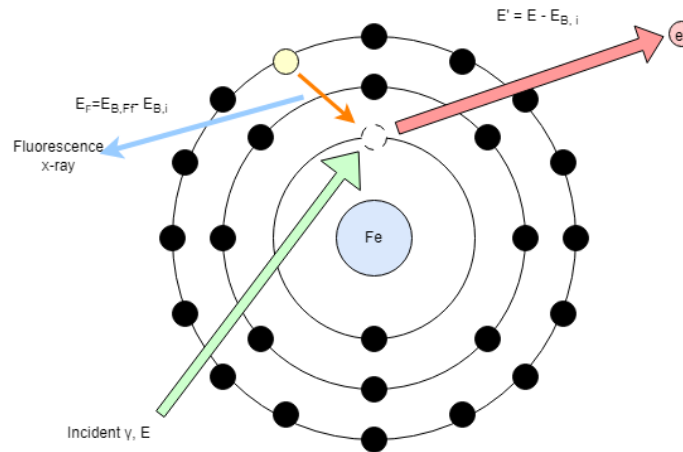

Figure 1.1: Depiction of x-ray fluorescence, from photo-absorption leading to the emission of a
photo-electron, to the subsequent filling of the vacancy by an upper shell electron.

Fluorescence x-rays are characterized based on the initial shell where the fluorescing electron is

situated before fluorescence and the final shell where the electron falls. For example, Kα x-rays are

x-rays arising from an electron from the L-shell (n = 2) dropping to fill a vacancy from an emitted K-shell (n = 1) photo-electron. On the other hand, $L\beta$ x-rays are x-rays arising from an N-shell (n = 4) electron dropping to fill a vacancy from an emitted L-shell (n = 2) photo-electron. It should be noted that emitted x-rays can also be absorbed by upper-shell electrons, which results in the emission of Auger electrons. The emission of K x-rays is more likely to occur for incoming energies just above the K-edge of a target atom, or the binding energies of K-shell electrons. As such, it is ideal to use sources that emit energies close to the K-edge of a target atom.

X-ray fluorescence in measuring trace element compositions is built around the fact that characteristic x-rays of elements have distinct energies. The unique atomic number of elements and consequent unique electron binding energies result in a characteristic x-ray series that is emitted from the element and unique to the element. The elemental composition of a sample can be determined by quantifying the number of x-rays at energies characteristic of specific elements. For example, iron $K\alpha$ and $K\beta$ x-rays are characterized as 6.40 and 7.06 keV, respectively. [19]

1.2.1   X-ray fluorescence for *in vivo* applications

X-ray fluorescence has an extensive range of applications. One of its most notable uses is in trace elemental detection *in vivo*.

Typically, IVXRF systems are distinguished based on the following criteria: the excitation source the system uses, the trace element being examined, the characteristic x-rays being explored, and the body part being measured. Sources which were originally used to detect lead in bone through XRF include ^{57}Co, ^{125}I, and ^{109}Cd. [20]

One of the first applications of IVXRF was detecting lead in bone. [21, 22, 23] IVXRF has grown in applicability since then. Some examples of systems that were developed are systems that detect strontium in bone, iron levels in the blood, and trace elements e.g. zinc in the skin. [24, 25, 26, 27]

1.3   Monte Carlo Computation

Monte Carlo simulations are an essential aspect of radiation research, as they allow an effective means of estimating the behaviour of radiation-based systems. The basis of Monte Carlo computation in the context of particle physics is that a random number is generated for every instance of a given particle, which then determines how the particle will behave for a specific stretch of time.[28] In the context of radiation science, Monte Carlo computation allows for an effective simulation of individual radiation particles, leading to an effective simulation of radiation-based systems and situations.

Applications of Monte Carlo computation include simulating scatter radiation in radiology [29], modelling radiotherapy treatment [30], and modelling absorbed dose [30, 31]. Typical transport code packages to use in building Monte Carlo simulations include Monte Carlo N-type Particle Transport (MCNP), Electron Gamma Shower (EGS), and GEometry ANd Tracking (GEANT).

1.4   Project Goal & Chapters of Overlap

This project investigates the applicability of an ^{125}I-based IVXRF system in measuring skin iron levels. ^{125}I is a radioisotope that is commonly used in medical procedures such as brachytherapy and, as such, is widely available for use. It has also been shown to be effective in other similar applications of IVXRF, making it an ideal excitation source for IVXRF systems. [25, 31, 32] This system aims to be a non-invasive, cheap, and effective alternative to current standards of measuring iron levels *in vivo*.

This project will discuss the experiments to characterize the IVXRF system, explore its feasibility to be applied *in vivo* through *ex vivo* measurements, and the simulation work done through Monte Carlo computation.

Chapter 2

2   Applicability of an ^{125}I-based *in vivo* x-ray fluorescence system in measuring skin iron

2.1   Chapter Outline

This chapter covers the paper *Applicability of an ^{125}I-based in vivo x-ray fluorescence system in measuring skin iron* verbatim. The authors of this paper are Bobby Tang, Sami Ullah Bangash, Fiona McNeill, and Michael Farquharson. All of the authors are affiliated with McMaster University.

In this paper, there are some areas of overlap with other chapters within this thesis. The content in the introduction section of the paper was explained in further detail in Chapter 1.

The methodology section of the paper is explained in further detail in Chapters 3 and 4 of the thesis.

The limitations section in the paper is expanded upon in further detail in Chapter 5.

Applicability of an ^{125}I-based *in vivo* x-ray fluorescence system in measuring skin iron

Bobby Tang[1], Sami Ullah Khan Bangash[1], Fiona E McNeill[1], and Michael J Farquharson[2]

[1] Department of Physics & Astronomy, McMaster University, Hamilton, ON, Canada
[2] School of Interdisciplinary Science, McMaster University, Hamilton, ON, Canada

E-mail: tangb12@mcmaster.ca

Abstract.
Background: Iron overload conditions are prevalent in global healthcare and require accurate monitoring of iron levels to provide treatment effectively. In recent years, x-ray fluorescence (XRF) measurement has emerged as a candidate point-of-care measurement tool for the detection of trace elements *in vivo* (IVXRF). This study explores the feasibility of a portable ^{125}I-based IVXRF instrument using as a point-of-care skin iron measurement device. **Methods:** The system was calibrated using iron-doped water phantoms for a range of physiologically-applicable iron concentrations. Measurements were conducted on *ex vivo* rat skin samples ($n = 34$), then correlated to measurements using a laboratory-based benchmark. Monte Carlo simulations were also performed to estimate its radiation dose to soft tissue. **Results:** For an 1800 s real-time measurement period, the system showed good precision with a minimum detectable limit (MDL) of 3.86 ± 0.06 ppm of iron. Measurements obtained by the IVXRF system were linearly correlated to benchmark measurements, suggesting good system accuracy. Importantly, measurements made by the IVXRF system were linearly correlated to rat-injected iron dose, indicating that the system can distinguish different iron levels in rats. The effective dose from the IVXRF system is 101.68 ± 0.03 nSv, meaning an *in vivo* measurement would be low risk. **Conclusion:** The system was shown to accurately measure iron concentrations in *ex vivo* rat skin samples within a physiologically-applicable range. Further work shall be conducted to validate the system in *in vivo* applications.

Keywords: *In vivo* x-ray fluorescence, Monte Carlo, Skin iron, iron overload

1. Background

1.1. Iron overload conditions

Iron overload conditions are a prevalent issue in global health. Conditions such as β-thalassemias and hereditary hemochromatosis affect a significant proportion of the worldwide population. [1, 2, 3] β-thalassemias are a group of conditions that arise from inhibited production of hemoglobin. [1] This inhibition results in anemia and other symptoms such as growth deficiencies, poor musculature, jaundice, and osteoporosis. [4] To improve the quality of life of thalassemic patients, patients can undergo blood transfusions to maintain a healthy hemoglobin count. [5] However, if not properly monitored, these transfusions can lead to iron overload, which can lead to symptoms such as diabetes and growth retardation. [6] Hemochromatosis occurs in response to a genetic mutation that affects *HFE* expression. This mutation leads to unregulated iron uptake in the intestines [7], resulting in iron overload. Symptoms from hereditary hemochromatosis include diabetes, hypothyroidism, osteoporosis, cirrhosis, and lethargy. [7]

If not properly treated, iron overload conditions can lead to iron buildup in organs such as the heart and liver. [8] Iron buildup in the heart can also lead to dysfunction of the heart, which in turn can lead to heart failure through restrictive cardiomyopathy and diastolic dysfunction. [9, 10]

1.2. Iron overload treatment

One of the primary treatments for iron overload from β-thalassemia is iron chelation therapy, as it allows the body to increase the excretion of excess iron. [11] The idea behind this treatment is that a chelating agent, e.g. deferoxamine (DFO), promotes the formation of complexes with iron, which the body can then excrete. The primary treatment for hereditary hemochromatosis is phlebotomy, or removing blood to lower iron levels, with iron chelation being an alternative treatment. [3, 12]

While chelation therapy has been shown to be effective in treating iron overload, patient iron levels must be monitored to quantify chelator efficiency. Liver biopsies are considered the gold standard of iron level assessment and are often used to diagnose hereditary hemochromatosis, but they are invasive and can lead to surgical complications. [8, 12] Magnetic resonance imaging (MRI) has been shown to be accurate in measuring iron levels, along with superconducting quantum interface devices (SQUIDs). However, these methods are expensive to maintain, and MRI techniques are continuing to be further optimized. [13, 14] One of the most common monitoring methods is by measurement of patient blood serum ferritin; however, they can be unreliable as ferritin levels tend to increase with inflammation. [15] In addition, while serum ferritin measurements can be performed in a day, they take longer to process than the duration of a patient appointment. Physicians must make follow-up appointments with patients to discuss the results, which can add an extra time burden on both the
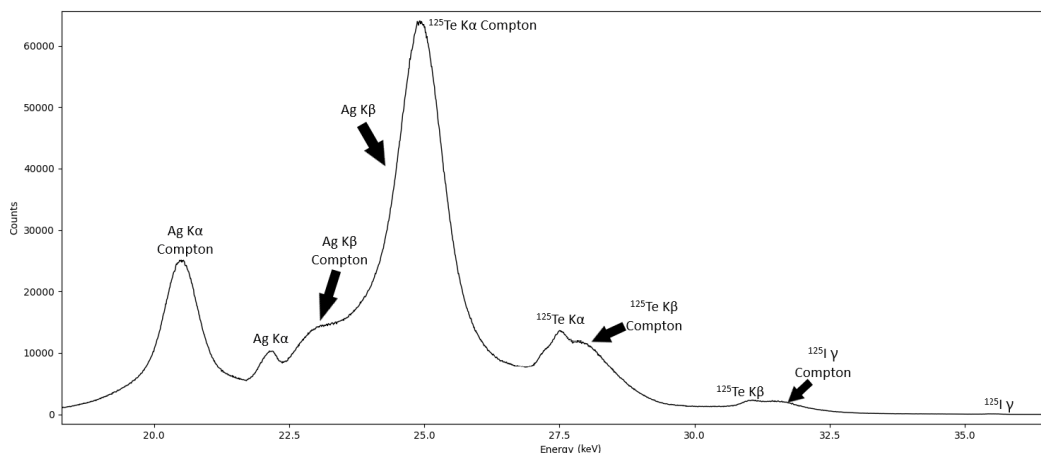
Figure 1: Backscatter spectrum of sources from the ^{125}I brachytherapy seeds.

patient and the physician. There is a need for an accurate, quick, cost-effective, and non-invasive point-of-care device for monitoring patient iron levels. This study describes the development of an *in vivo* ^{125}I-based XRF system for measuring iron in skin as a potential surrogate measure for body iron burden.

2. Methods

2.1. Detector System

The system is designed around a KETEK AXAS-M detector that employs a VITUS H150 silicon drift detector (SDD) module. The VITUS H150 has a 170 mm^2 SDD chip collimated to a 150 mm^2 active area, an absorption depth of 450 μm of Si, and an energy resolution of $\leq$ 136 eV for energy ranges of 0.2-30 keV. The optimal peaking time of the SDD is 1 μs, and the maximum input count rate of the detector is 2 Mcps. The detector has a 25 μm thick beryllium window seal to maintain a vacuum seal and block incoming charged particle signals.

2.2. ^{125}I Source

Three iodine-125 (^{125}I) brachytherapy seeds from IsoAid^{TM}, each with an activity of 0.6 mCi (for a total of 1.8 mCi, or 66.6 MBq) were used as the excitation source for the system. ^{125}I has a half-life of 59.5 days, and it emits coherent γ rays at 35.49 keV. ^{125}I undergoes decay through electron capture, which results in its decay to ^{125}Te. The brachytherapy seeds comprise of ^{125}I in the form of silver iodide (AgI) surrounded by silver markers enclosed in a titanium capsule. [16] Due to these silver markers and the AgI, the seeds also emit Ag Kα and Kβ x-rays. Table 1 shows the energies and frequencies for source photon emissions. Figure 1 shows the backscatter spectrum of the ^{125}I seeds in a typical calibration experiment.

Table 1: Key photon emissions from ^{125}I seeds. [17, 18, 19]

Element	Emission Type	Energy (keV)	Emission (per decay)
[125]I	γ	35.49	0.0668
[125]Te	Kβ x-ray	31.704	0.0381
		30.99	0.132
		30.94	0.0683
	Kα x-ray	27.47	0.757
		27.202	0.406
Ag	Kβ x-ray	24.94	0.0752
		24.912	0.039
	Kα x-ray	22.16	0.456
		21.99	0.242
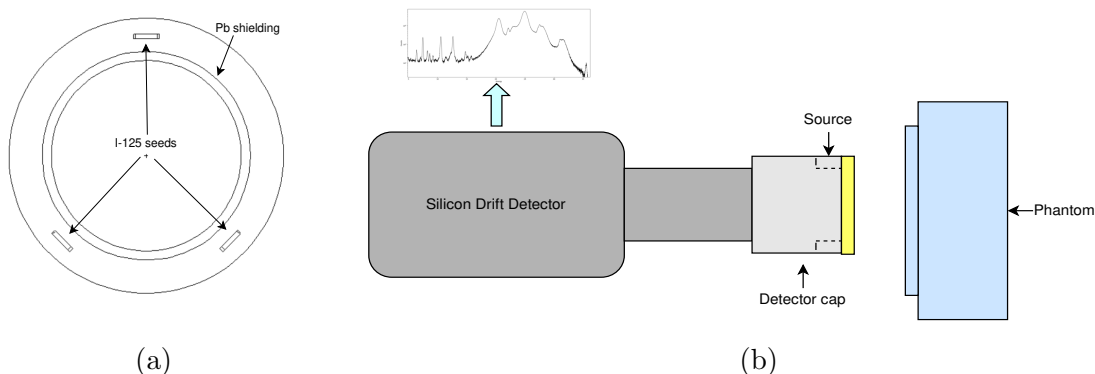
Figure 2: Aluminum cap source holder (left) and calibration experiment setup (right). Note the backscatter geometry of the experiment. [20]

2.3. Aluminum cap and source holder

An aluminum detector cap was designed for the system. The cap has three 1.2 mm deep cylindrical holes on its edge that house the ^{125}I seeds. The seeds are sealed by a 0.25 mm thick styrene layer that rests on top of the cap to ensure the seeds stay in place. While the styrene will attenuate source particles towards the target and x-rays from the target, the layer also helps keep the ^{125}I seeds in the cap while protecting the detector's beryllium window. The layer is also cleaned to prevent signal contamination. The aluminum cap has a 1 mm lead layer within its inner bore, which lowers the detector dead time by attenuating [125]I γ rays and silver & tellurium x-rays from the source seeds. Figure 2a shows the system cap, inner lead shielding, and holes that fit the ^{125}I seeds.

2.4. Phantoms

Iron-doped water calibration phantoms were employed to minimize variability in establishing a calibration curve. The phantoms are made of PLA plastic, and the

solutions are sealed by a 4 μm ultralene XRF film window. These phantoms have been shown to ensure measurement reproducibility by reducing geometric variation. [21] The phantoms have a volume of 25 mL and are filled with solutions of varying concentrations of iron nitrate (FeNo$_3$).

2.5. Calibration

Calibration was performed using phantoms with 0 to 400 ppm of iron-doped water solution. Each phantom was measured 5 times for an acquisition time of 1800 s real-time. This run time allowed for a low detection limit and repeating the measurement 5 times allowed for a standard deviation to be calculated for each concentration. The peak fitting of spectral emission peaks to Gaussian distribution curves was conducted using PyMCA fitting software. This peak fitting was done to determine the areas of the iron Kα and nickel Kα x-ray peaks for each measurement. After spectra analysis, a calibration curve was established between phantom iron concentration in ppm and the iron counts normalized to nickel counts. The iron signal was normalized to account for the varying activity of the ^{125}I sources between different measurement days due to its short half-life. In addition, the nickel Kα peak is prominent in the collected spectra, as the detector comprises of nickel. Linear regression analysis was conducted to determine the slope and intercept of the calibration line. Figure 2b shows the experimental setup of the calibration experiments.

With the calibration curve established, the system's minimum detectable limit (MDL) was determined using 1. σ_{0ppm} is the standard deviation associated with the 0 ppm phantom, and m is the slope of the calibration line. [22]

$$MDL = \frac{2\sigma_{0ppm}}{m} \tag{1}$$

Calibration lines were established for both the Kα and Kβ x-rays. By using 2, the overall system minimum detectable limit for iron can be calculated.

$$\left(\frac{1}{MDL}\right)^2 = \left(\frac{1}{MDL_{K\alpha}}\right)^2 + \left(\frac{1}{MDL_{K\beta}}\right)^2 \tag{2}$$

2.6. Rat skin samples & laboratory XRF system

Rat skin samples previously prepared and measured in studies by Dao et al. [23] were measured using our portable *in vivo* XRF system. The original study has been fully described elsewhere. [23] To briefly summarize, male Wistar rats weighing 126-150g were injected with varying amounts of iron dextran over 3 to 4 weeks. After the injection period, the rats underwent an 8-day equilibration period. Rats were then sacrificed, and skin samples were obtained. The rat skin samples were measured using a benchmark laboratory XRF system. The laboratory system is a measurement system designed explicitly for measuring tissue. Table 2 shows the details of the ingested iron levels of the rats from the initial study.

Table 2: Rat skin sample groups and administered iron levels.

Iron Level	Total iron intake (mg Fe^{2+})	Samples measured
Low	0	9
	45	3
Medium	60	1
	75	2
	80	7
	120	1
High	160	11
Total		34

Measurements of the rat skin samples using the ^{125}I-based XRF system were conducted using the same method as the calibration experiments. The rat skins were prepared and placed on the window of a blank calibration phantom. The rat skin phantoms had a 1 cm thick wax layer behind the skin instead of water to create an x-ray scattering environment similar to the calibration phantoms. Wax was used instead of water because the rat skins could be more readily affixed to the firmer material. After the rat skins were measured, their spectra were analyzed as per the calibration phantoms, where the normalized iron Kα signal was collected for each sample.

It should be noted that iron counts from the benchmark system are normalized to the argon Kα x-ray counts. This is because the benchmark system's spectra present a strong argon Kα, as shown in figure 3.

Linear regression was conducted for the IVXRF signal with respect to the laboratory XRF signal. To account for the uncertainty in both systems, linear regression was also conducted in the other direction for the laboratory XRF signal with respect to the IVXRF signal. Structural analysis was then conducted to form a range of regressions within which the actual regression between the two systems lies.

The rat skin samples were also divided into three treatment groups: low (0-45 mg of injected Fe^{2+}), medium (60-120 mg of injected Fe^{2+}), and high (160 mg of injected Fe^{2+}). The three rat skin treatment groups were compared using t-tests to quantify the difference in detected iron counts between each group. Linear regression was also performed between the rat-injected iron dose and the IVXRF iron signal to determine if the IVXRF system can distinguish between different iron doses in *ex vivo* rat skin samples.

2.7. Monte Carlo simulations

Monte Carlo N-Particle Transport (MCNP6.2) was used to develop Monte Carlo models of the system. These simulations aimed to better quantify the interactions of the IVXRF system with soft tissue by simulating the geometry and x-ray events in a

typical measurement. To simulate the sources, 3 isotropic volumetric sources similar in dimension to the ^{125}I seeds were made. These sources emitted photons with energies and emission rates as defined by the American Association of Physicists in Medicine (AAPM) for ^{125}I seeds. [16, 24]

To quantify the effects of the depth of iron on the detected iron signal strength, Monte Carlo simulations were performed of a soft tissue sample with a 1 mm thick iron layer. This layer was located at different depths, ranging from the surface of the sample (d = 0 mm) to 3 mm within the sample (d = 3 mm) at intervals of 0.2 mm.

In addition, the Monte Carlo models were used to estimate the dose to skin and other soft tissues from the ^{125}I-based IVXRF system on soft tissue. Doses were calculated for a simulated 1800 s measurement for a soft tissue target, and doses were calculated as defined by ICRU 44. [25] Monte Carlo simulations have been shown to be effective in simulating the absorbed dose of ^{125}I seeds in soft tissue. [26, 27]

To provide further validation of the results of the Monte Carlo simulations, an analytical calculation for absorbed dose was done using 3. $\dot{D}$ is the dose rate in Gy/s, $\dot{\Phi}_i$ is the energy fluence rate of a particular photon i, and $(\mu_{en}/\rho)_i$ is the mass energy-absorption coefficient of photon i within soft tissue. [28, 29]

$$\dot{D} = \sum_i \dot{\Phi}_i \left(\frac{\mu_{en}}{\rho}\right)_i \tag{3}$$

This calculation can only be an approximation but permits some verification of Monte Carlo simulations. The appropriate weighting factors from ICRP 103 were used to estimate the effective dose. [30] For this approximate analytical calculation, a measurement time of 1800 s was used, the source was assumed to be a single isotropic point source 1 cm away from the tissue, and the activity was assumed to be 0.6 mCi per seed, leading to a total activity of 1.8 mCi. The calculation assumes that the target is thin compared to the mean free path of the source photons, and as such, it does not account for attenuation within the sample. [28] As such, this calculation is expected to overestimate the actual dose.

3. Results

3.1. Calibration line

Figure 3a shows the IVXRF system spectrum. The Fe Kα (6.40 keV) and Kβ (7.06 keV) peaks are x-ray fluorescence peaks emitted from the target towards the detector. Ni Kα (7.48 keV) and Kβ (8.26 keV) peaks are observed and arise from x-ray fluorescence events between photons incident on the detector and the nickel cap surrounding the SDD. Pb Lα (10.5 keV) and Lβ (12.6 keV) peaks arise from source photons interacting with lead shielding within the aluminum cap.

Figure 3b shows the benchmark laboratory XRF system spectrum. The laboratory XRF spectrum has observable peaks similar to the *in vivo* XRF spectrum, such as the Fe Kα and Kβ peaks, as well as the Ni Kα and Kβ peaks. The most notable difference is the
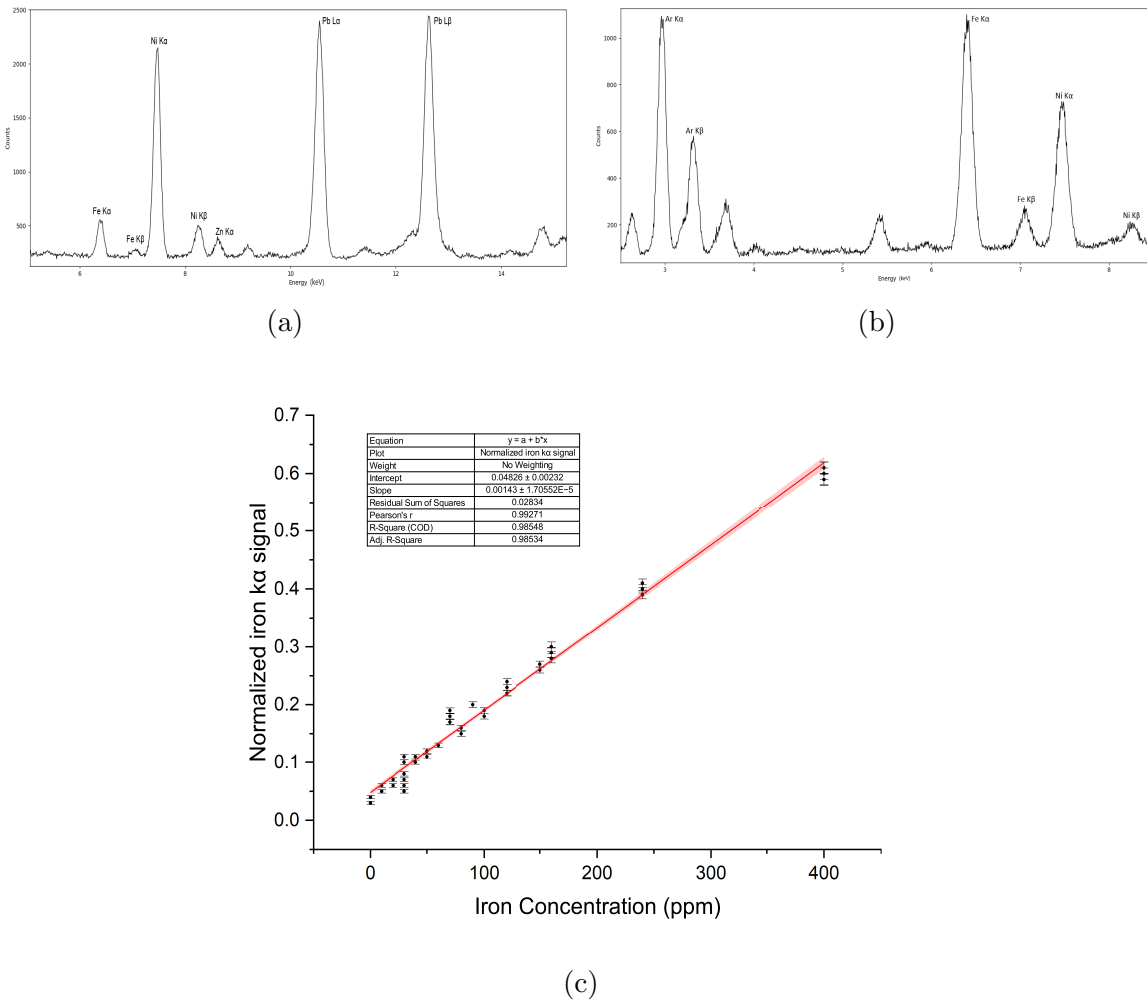
(a)

(b)

(c)

Figure 3: *In vivo* XRF (top-left), laboratory XRF system (top-right) spectra, and calibration line (bottom) of the IVXRF system using water phantoms with varying iron concentrations from 0 ppm to 400 ppm. The 95% confidence limits of the calibration line are shown.

presence of Ar Kα (2.96 keV) and Kβ (3.19 keV) peaks that arise due to the laboratory system's focused beam interacting with argon in the atmosphere of the enclosed system.

Figure 3c shows the calibration line obtained from the ^{125}I IVXRF system from water-based phantoms. The reported uncertainties for the calibration line are associated with the Poisson measurement uncertainties of the x-ray peaks. The dead time for measurements was found to be in the range of 10-15 %. The measured signal ratio and iron concentration are highly correlated, and the slope is highly significant ($p < 0.01$). The R^2 value for the calibration line of iron concentration in ppm to normalized iron signal is 0.985.

From figure 3c, we determined the calibration line equation of the normalized iron signal to the phantom iron concentration in ppm. This equation can be rearranged to determine the iron concentration of unknown samples if the normalized iron signal is
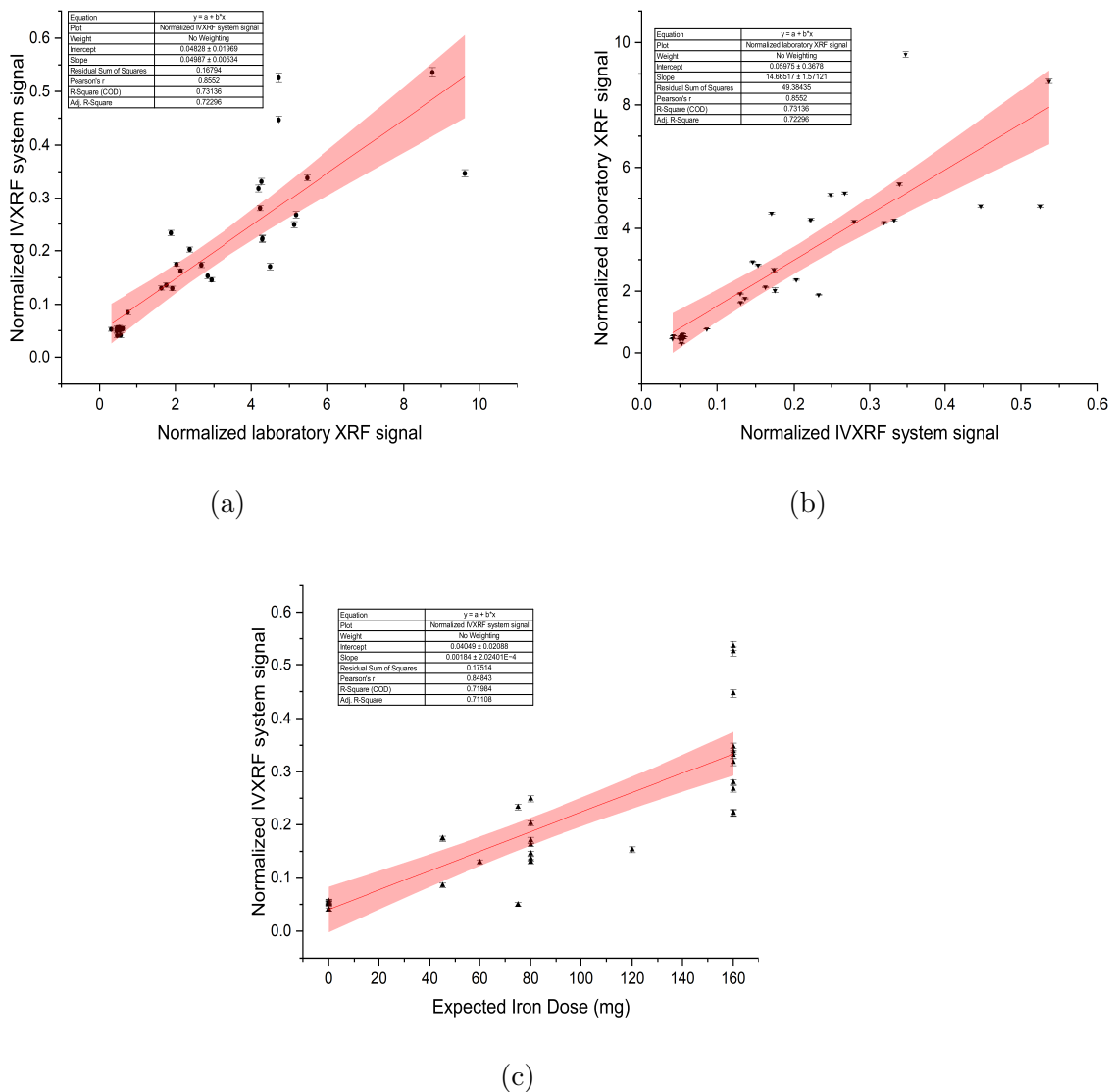
(a)

(b)

(c)

Figure 4: Linear regressions of the IVXRF iron signal with respect to the benchmark iron signal (left-top), the benchmark iron signal to the IVXRF iron signal (right-top), and the IVXRF iron signal to the rat sample iron treatment (bottom). The 95% confidence limits are shown.

known. Using 1, the MDL of the x-ray fluorescence system was found to be 3.86 ± 0.06 ppm of iron.

Using 2, the iron Kβ peak was explored. However, due to interference from the nickel Kα peak, the iron Kβ peak was not explored further in this study. This is because it did not significantly impact the system's total MDL.

Table 3: T-test results comparing the iron signals of the different treatment groups.

	t-value	p-value	95% CI
Low & Medium	4.001	< 0.01	$0.038 - 0.134$
Low & High	7.644	< 0.01	$0.195 - 0.355$
Medium & High	5.091	< 0.01	$0.106 - 0.271$

3.2. Ex vivo measurements

Figures 4a and 4b show the linear regression between the normalized rat skin iron signals from the IVXRF system and the normalized rat skin iron signals from the laboratory XRF system. Using the calibration curve equation determined earlier, the rat skins were measured to have iron concentrations of -3.62 to 342.89 ppm. The range within which the true linear regression lies is shown below by performing structural analysis with both regressions.

$$\left(\frac{Fe}{Ni}\right) = (0.06 \pm 0.02) \times \left(\frac{Fe}{Ar}\right) + (0.02 \pm 0.05) \tag{4}$$

Table 3 compares normalized iron counts between the different treatment groups. The t-values describe the significance of the differences between the treatment groups' mean iron signals. The 95% confidence intervals represent the range of the difference between the two groups.

Figure 4c shows the regression of the IVXRF system's signal to sample iron-injected dose. The normalized signal and injected iron dose are highly correlated ($R^2 = 0.7198$), and the measured slope is highly significant ($p < 0.01$).

3.3. Monte Carlo Simulation

Figure 5 shows the relation between the normalized iron signal from Monte Carlo simulations with respect to the depth of a 1 mm iron layer in a soft tissue target. The graph shows how the iron depth in the target can affect the detected iron signal.

Table 4: Simulated absorbed dose to a tissue target at varying distances from the source.

Distance from source (cm)	Simulated absorbed dose (mGy)
0.5	8.735 ± 0.002
1.0	6.832 ± 0.002
2.0	4.356 ± 0.002
4.0	2.116 ± 0.001

Table 4 shows the dose in a soft tissue target at varying distances from the IVXRF source in the Monte Carlo simulations. Using 5, the effective dose, E, can be calculated,
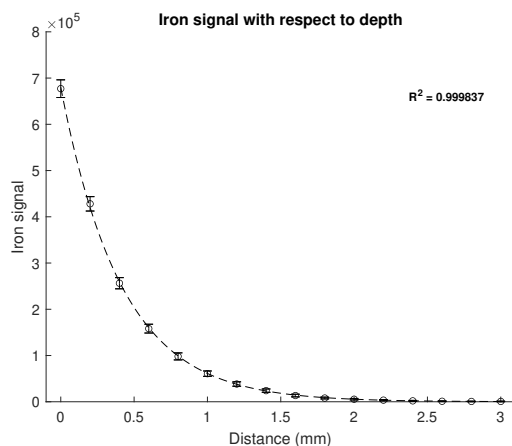
Figure 5: Curve of MCNP-simulated iron signal with respect to the depth of a 1 mm iron layer within a soft tissue target.

given that the radiation weighting factor, w_r, of photons is 1, and the tissue weighting factor of skin, w_t, is 0.01. [30] The total skin surface was taken to be equal to that of the reference man as cited in ICRP 89. [31] It was assumed that only the dose to skin was significant, and as such, the dose to other organs in the body was not considered,

$$E = \Sigma_{n=1}^{i} D_i w_r w_i \frac{volume_{irradiated,i}/d}{surface_{total,i}} \tag{5}$$

4. Discussion

4.1. Minimum detectable limit

The ^{125}I-based *in vivo* x-ray fluorescence system's phantom-based MDL was found to be 3.86 ± 0.06 ppm of iron. The MDL suggests that the system will be able to measure the skin iron levels of both thalassemic and healthy patients. Previous studies suggest iron ranges of 5.6-14.0 ppm of iron in healthy patients and iron ranges of 13.0-150 ppm in β-thalassemic patients. [32] Further, the MDL may also suggest that the system could theoretically measure into the higher end of the iron deficient range.

4.2. Ex vivo rat skin measurements

From Figures 4a and 4b, the R^2 value for the linear regressions between the IVXRF rat skin iron signal and the laboratory XRF rat skin iron signal is 0.731. This R^2 value suggests a strong positive correlation between the signals produced from both systems. The p-value of the slope is less than 0.01, which suggests that the regression is statistically significant. These results indicate that the IVXRF system can measure skin iron levels *in vivo* in rats with good precision.

Similar to the phantom measurements, the reported uncertainties from the rat skin measurements are those associated with the Poisson measurement uncertainties of the

x-ray peaks. It should be noted that additional uncertainties are associated with the biological variation within the samples, such as how each rat metabolized the injected iron. [23] However, these biological uncertainties cannot be quantified.

From table 3, the t-test p-values between the low & medium iron, low & high iron, and medium & high iron treatment groups are statistically significant with $p < 0.01$. From figure 4c, the R^2 value of the regression of the IVXRF signal to sample iron treatment is 0.719, suggesting a strong positive correlation between the injected iron of each sample and its corresponding iron signal strength. The p-value of the slope is less than 0.01, which suggests that the regression is statistically significant. These results, and those from table 3 indicate that the IVXRF system can distinguish the skin iron concentrations of different iron treatments within *ex vivo* rat samples.

4.3. Monte Carlo & Dosimetry

Figure 5 shows that the depth distribution curve could be fitted by an exponential decay relationship with $R^2 > 0.99$. This relationship shows a significant drop-off in iron detection with the depth of the iron layer as expected, suggesting that the simulation can accurately simulate an XRF measurement using the system.

From the MCNP simulations, the simulated absorbed dose for a soft tissue target 1 cm away from the IVXRF system is 6.832 ± 0.002 mGy. Using 5, the effective dose for a soft tissue target 1 cm from the system was 101.68 ± 0.03 nSv. These results align with the dosimetry results from previous publications that have explored ^{125}I as an excitation source in similar applications of *in vivo* x-ray fluorescence. [26, 27] The analytical effective dose calculation using 3 and accounting for weighting across the entire body is 337.16 nSv. The analytical calculation is considered an overestimation of the system's effective dose, as it does not account for attenuation of the incident particles within the target.

In the context of the average person's radiation exposure, the average annual effective dose due to natural radiation sources is 2.4 mSv per year. [33] In the context of diagnostic imaging, the average chest x-ray taken from the posteroanterior view yields an effective dose of 0.11 mSv. [34] This dose is thus extremely low.

5. Conclusion

The ^{125}I-based x-ray fluorescence system was shown to be feasible in measuring *in vivo* skin iron levels in rats. It results in a low MDL and dose within a reasonable 1800s real-time measurement period. However, there is still further work that should be conducted to improve and validate the system before it can proceed to human measurements. Improvements in the system could include the addition of a collimator to lower inadvertent dose, increasing the activity of the ^{125}I seeds to lower the system MDL, and adjusting the pulse processing chain of the detector to minimize the system dead time. Further studies looking into comparisons with other forms of elemental analysis,

like inductively coupled plasma mass spectrometry (ICP-MS), would aid in further verifying the accuracy of the system. [35] Comparing measurements using dosimetry chips with simulation results would validate the simulation and the expected dose from the IVXRF system. That said, while further improvements could improve the system, it shows potential to be an effective, non-invasive point-of-care instrument.

Ethics statement

Not applicable

Availability of data and materials

The data that support the findings of this study are available upon reasonable request from the authors.

Competing interests

Not applicable

Funding

Acknowledgments

References

[1] R. Galanello and R. Origa. Beta-thalassemia. *Orphanet journal of rare diseases*, 5:1–15, 2010.

[2] R. E. Fleming and P. Ponka. Iron overload in human disease. *New England Journal of Medicine*, 366(4):348–359, 2012.

[3] A. Pietrangelo. Hereditary hemochromatosis—a new look at an old disease. *New England Journal of Medicine*, 350(23):2383–2397, 2004.

[4] R. Origa. β-thalassemia. *Genetics in Medicine*, 19(6):609–619, 2017.

[5] Y. Aydinok. Thalassemia. *Hematology*, 17(sup1):s28–s31, 2012.

[6] N. Shah, A. Mishra, D. Chauhan, C. Vora, and N. R. Shah. Study on effectiveness of transfusion program in thalassemia major patients receiving multiple blood transfusions at a transfusion centre in western india. *Asian journal of transfusion science*, 4(2):94, 2010.

[7] B. K. Crownover and C. Covey. Hereditary hemochromatosis. *American family physician*, 87(3):183–190, 2013.

[8] A. Pietrangelo. Hereditary hemochromatosis: pathogenesis, diagnosis, and treatment. *Gastroenterology*, 139(2):393–408, 2010.

[9] D. T. Kremastinos, D. Farmakis, A. Aessopos, G. Hahalis, E. Hamodraka, D. Tsiapras, and A. Keren. β-thalassemia cardiomyopathy: history, present considerations, and future perspectives. *Circulation: Heart Failure*, 3(3):451–458, 2010.

[10] C. J. Murphy and G. Y. Oudit. Iron-overload cardiomyopathy: pathophysiology, diagnosis, and treatment. *Journal of cardiac failure*, 16(11):888–900, 2010.

[11] N. F. Olivieri and G. M. Brittenham. Iron-chelating therapy and the treatment of thalassemia. *Blood, The Journal of the American Society of Hematology*, 89(3):739–761, 1997.

[12] C. Borgna-Pignatti and M. Marsella. Iron chelation in thalassemia major. *Clinical therapeutics*, 37(12):2866–2877, 2015.

[13] J. C. Wood. Use of magnetic resonance imaging to monitor iron overload. *Hematology/Oncology Clinics*, 28(4):747–764, 2014.

[14] D. Hernando, Y. S. Levin, C. B. Sirlin, and S. B. Reeder. Quantification of liver iron with mri: state of the art and remaining challenges. *Journal of Magnetic Resonance Imaging*, 40(5):1003–1021, 2014.

[15] A. Dignass, K. Farrag, and J. Stein. Limitations of serum ferritin in diagnosing iron deficiency in inflammatory conditions. *International journal of chronic diseases*, 2018, 2018.

[16] M. J. Rivard, W. M. Butler, L. A. DeWerd, M. Saiful Huq, G. S. Ibbott, A. S. Meigooni, C. S. Melhus, M. G. Mitch, R. Nath, and J. F. Williamson. Supplement to the 2004 update of the aapm task group no. 43 report. *Medical physics*, 34(6Part1):2187–2205, 2007.

[17] J. Katakura. Nuclear data sheets for a = 125*. *Nuclear Data sheets*, 112:497–705, 2010.

[18] J. Blachot. Nuclear data sheets for a = 107. *Nuclear Data Sheets*, 109(6):1383–1526, 2008.

[19] S. Y. F. Chu, L. P. Ekström, and R.B. Firestone. The lund/lbnl nuclear data search.

[20] M. Zamburlini, A. Pejović-Milić, and D. R. Chettle. Evaluation of geometries appropriate for ^{125}i *in vivo* bone strontium x-ray fluorescence measurement. *Journal of radioanalytical and nuclear chemistry*, 269(3):625–629, 2006.

[21] S. U. K. Bangash, F. E. McNeill, M. J. Farquharson, and D. R. Chettle. Feasibility of a ^{109}cd-based portable xrf device for measuring skin iron concentration in anaemic and β-thalassaemic patients. *Biomedical Physics & Engineering Express*, 8(6):065034, 2022.

[22] H. Hu, A. Aro, and A. Rotnitzky. Bone lead measured by x-ray fluorescence: epidemiologic methods. *Environmental Health Perspectives*, 103(suppl 1):105–110, 1995.

[23] E. Dao, M.P. Zeller, B.C. Wainman, and M.J. Farquharson. Feasibility of the use of a handheld xrf analyzer to measure skin iron to monitor iron levels in critical organs. *Journal of Trace Elements in Medicine and Biology*, 50:305–311, 2018.

[24] M. J Rivard, B. M. Coursey, L. A. DeWerd, W. F. Hanson, M. Saiful Huq, G. S. Ibbott, M. G. Mitch, R. Nath, and J. F. Williamson. Update of aapm task group no. 43 report: A revised aapm protocol for brachytherapy dose calculations. *Medical physics*, 31(3):633–674, 2004.

[25] ICRU. Tissue substitutes in radiation dosimetry and measurement. no. 4. *Radiology*, 173(1):202–202, 1989.

[26] M. Zamburlini, A. Pejović-Milić, D. R. Chettle, C. E. Webber, and J. Gyorffy. In vivo study of an x-ray fluorescence system to detect bone strontium non-invasively. *Physics in Medicine & Biology*, 52(8):2107, 2007.

[27] R. C. N. Studinski, F. E. McNeill, D. R. Chettle, and J. M. O'Meara. Estimation of a method detection limit for an in vivo xrf arsenic detection system. *Physics in Medicine & Biology*, 50(3):521, 2005.

[28] J. E. Turner. *Atoms, radiation, and radiation protection*. Wiley-VCH, third edition, 2008.

[29] J. H. Hubbell and S. M. Seltzer. Tables of x-ray mass attenuation coefficients and mass energy-absorption coefficients 1 kev to 20 mev for elements z = 1 to 92 and 48 additional substances of dosimetric interest. 5 1996.

[30] ICRP. Icrp publication 103. *Annals of the ICRP*, 37(2.4):2, 2007.

[31] ICRP. Icrp publication 89. *Annals of the ICRP*, 32(3-4):1–277, 2002.

[32] R. Gorodetsky, E. Loewenthal, A. Goldfarb, and E. A. Rachmilewitz. Non-invasive evaluation of

iron load and clearance in patients with β-thalassemia. *Annals of the New York Academy of Sciences*, 612(1):568–572, 1990.

[33] M. Charles. Unscear report 2000: sources and effects of ionizing radiation, 2001.

[34] M. I. Balonov and P. C. Shrimpton. Effective dose and risks from medical x-ray procedures. *Annals of the ICRP*, 41(3-4):129–141, 2012.

[35] R. S. Amais, G. L. Donati, and M. A. Zezzi Arruda. Icp-ms and trace element analysis as tools for better understanding medical conditions. *TrAC Trends in Analytical Chemistry*, 133:116094, 2020.

Chapter 3

3 Experimental Methods - Details

3.1 Chapter Overview

This chapter covers details of the experiment that were not discussed in Chapter 2. This section seeks to provide additional context on the experimental setups.

3.2 Detector System

As discussed in Chapter 2, the IVXRF system is designed around a KETEK AXAS-M detector system that employs a VITUS H150 silicon drift detector (SDD). The detector model was designed to analyze x-rays in the low-energy range and is considered ideal for energy ranges of 0.2 to 30 keV, as these models have a high quantum efficiency in the energy range of 2-30 keV. Silicon is also ideal for photon absorption measurements, as the photoelectric process is more prominent than Compton scattering in silicon for energies below 55 keV. [18] The system has a power supply unit that allows for signal processing and connects the system to a laptop with spectral analysis software. The detector head comprises a nickel-plated aluminum housing that connects the SDD to the power supply. Figure 3.1 shows the detector system and aluminum cap.
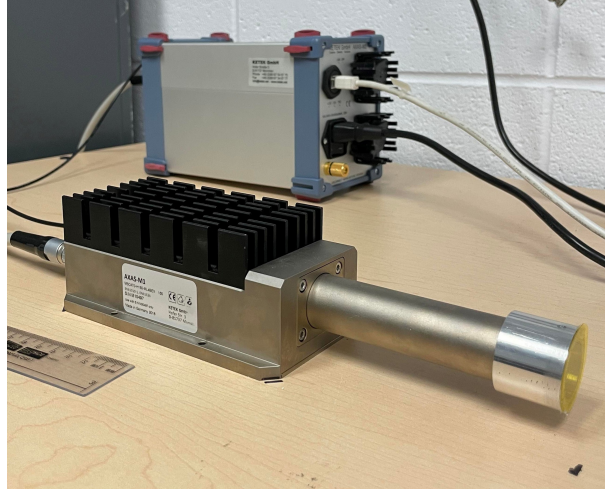
Figure 3.1: Silicon drift detector (SDD) used for the IVXRF system. The unit comprises a detector

head and signal processing unit.

The system uses a custom-made aluminum cap as the source holder for the ^{125}I seeds. The cap

was made to fit onto the detector head of the AXAS-M system while also protecting the beryllium

window of the VITUS H150 from external influences. The cap also had a 0.25 mm styrene layer taped

over the seed holes. While this layer led to some attenuation of iron x-rays, it kept the ^{125}I seeds

in place during measurements, and it also aided in protecting the beryllium window of the system.

From Equation 2, given that the mass attenuation factor of 6.4 keV x-rays through polystyrene is

8.9544 cm^2/g, and assuming a density of about 1 g/cm^3, it was found that the styrene window

resulted in a transmission rate of iron kα x-rays of roughly 80%. [33] Figure 3.2 shows the front view

of the aluminum cap.

$$A = A_0 exp[-(8.9544 \ cm^2/g)(1 \ g/cm^3)(0.025 \ cm)] = 0.8A_0 \qquad (2)$$
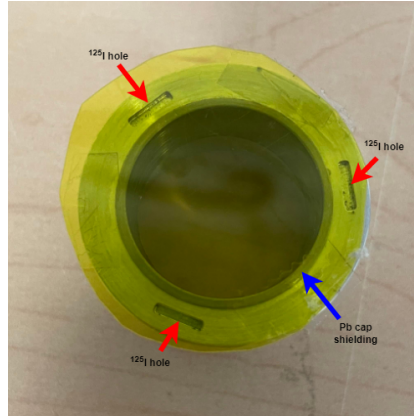
Figure 3.2: Front view of the aluminum source holder. Note the three holes to fit the ^{125}I seeds.

Figure 3.3 shows the experimental setup of the calibration and *ex vivo* rat skin measurements. A distance of 1 cm between the front of the cap and the target (an approximate 2 cm detector face-target distance) was chosen as it allowed for a high count rate from the source. Measurements were selected to take around 1800 s of real-time. This measurement acquisition time was found to provide a low minimum detectable limit (MDL) while minimizing the potential absorbed dose from the system. Figure 3.3 shows the experimental setup of the system.
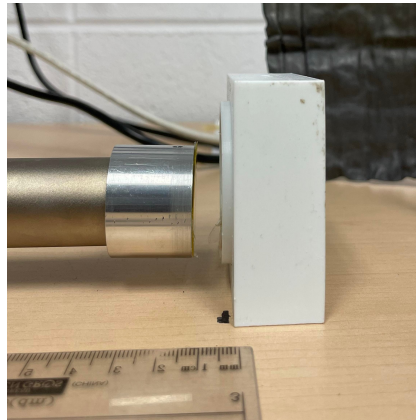

Figure 3.3: Experimental setup of the calibration and *ex vivo* measurements. The detector face-phantom distance is ≈ 2 cm.

3.3   Huber X-ray Fluorescence System

The Huber X-ray Fluorescence system is a laboratory-based bulk tissue measurement system at MacMaster University. Similar to the IVXRF system, the Huber comprises a KETEK AXAS-M detector system incorporating a VITUS SDD to detect radiation events. In addition, the Huber also allows for a controlled measurement environment. As such, it was chosen to be the reference standard against which the IVXRF system could be compared.

3.4   *Ex vivo* rat skin preparation

Rat skin samples were cut for measurement with the IVXRF system. This ensured they fit into the experimental sample holders. A sample holder similar in dimensions to the phantoms used in the calibration measurements was used to hold the rat skin samples. The samples were cut into circles with a diameter of 6 cm to fit them within the sample holder. They were wrapped in 4 μm thick ultralene XRF film and secured with tape to prevent contamination while minimizing interference with sample measurements. The skin samples were also shaved to ensure that rat fur did not contribute any confounding variables within measurements.

A wax layer was added behind the skin samples within the sample holder, as it allowed for a similar scattering environment to water, and was thus a better comparison to the calibration phantoms. In addition, the wax allows the samples to be more easily affixed within the sample holder than water. Figure 3.4 shows a sample wrapped in XRF film, Figure 3.5 shows the underlying wax used to affix the rat skin samples, and Figure 3.6 shows a mounted sample in the sample holder.

Figure 3.4: Rat skin sample after preparation.

Figure 3.5: Sample holder used for *ex vivo* sample measurement. Notice the wax fitted within the

phantom, which was added to ensure a similar scattering environment to water.

Figure 3.6: Sample holder with mounted rat skin sample over wax layer.

3.5   Conclusion

This chapter provided details of the calibration and *ex vivo* experiments that were not originally included in the submitted paper due to length restrictions and journal formatting. This chapter is intended to be read as an adjunct to the submitted article to provide further context and details regarding the experiments done in this study.

Chapter 4

4 Monte Carlo Simulation - Details

4.1 Chapter Overview

This chapter covers the work done to create models of the IVXRF system using Monte Carlo N-type Particle Transport (MCNP) code package. These simulations aided in estimating the behaviour of the system in different geometries, as well as in estimating the radiation dose of the system to the soft tissue of the skin.

4.2 Simulation geometry

To simulate the behaviour of the IVXRF system, its geometry was modelled within MCNP6.2. The detector face geometry in the simulations was built to resemble the geometry of the VITUS H150 SDD module that rests within the KETEK AXAS-M detector. The module comprises a silicon chip with a 150 mm^2 active area and a nickel layer to encapsulate the module. The module also had a 25 μm thick beryllium window seal in front of the silicon chip and a vacuum space between the seal and the detector face. The aluminum cap was also modelled, along with the polystyrene window on its front, the lead shielding within its inner bore, and three sources in the cap to simulate the three ^{125}I seeds. Figure 4.1 shows the simulated geometry in MCNP of the aluminum cap and VITUS H150 SDD module.
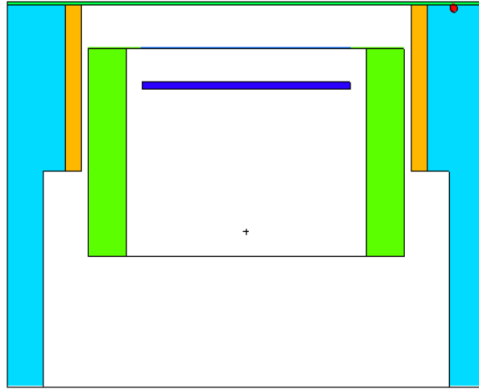
Figure 4.1: Simulation geometry of the SDD and aluminum cap. The cap (light blue) encapsulates the nickel overlay of the SDD (light green), which has a silicon chip (blue) meant to simulate the active volume of the detector and a thin beryllium window. The cap also comprises a styrene layer (green), source holder holes within the cap (red), and lead shielding (yellow).
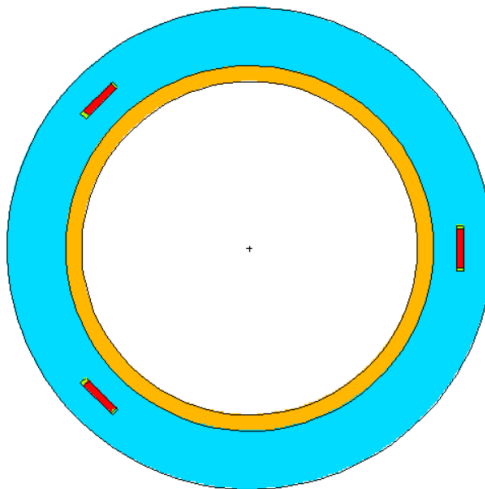

Figure 4.2: Front view of the aluminum cap. Each of the three sources along the cap's outer edge is made of silver iodide (red) and silver markers (green) along their sides.

Within the simulations, the three ^{125}I seeds were modelled using three isotropic volumetric sources similar in dimension to the ^{125}I seeds. The simulated sources are made of silver iodide, with silver markers along the ends of the seeds. [34] The sources emit photons with energies and frequencies following the protocol for simulating 125I seeds outlined by the American Association of Physicists in Medicine (AAPM). [35] Figure 4.2 shows the simulated geometry of the aluminum cap.

The simulation targets adopted a cylindrical shape meant to resemble the volume within the phantoms that would hold the targets in the experiments (the iron-doped water solutions during the calibration experiments and rat skin & wax during the *ex vivo* experiments). The target dimensions were set at a radius of 3 cm and a height of 2.5 cm. The simulations utilized a target made of a four-component soft tissue-equivalent material of hydrogen, carbon, nitrogen, and oxygen as defined by the ICRU. [36] Figures 4.3, 4.4, and 4.5 show the geometry of the dosimetry simulations.
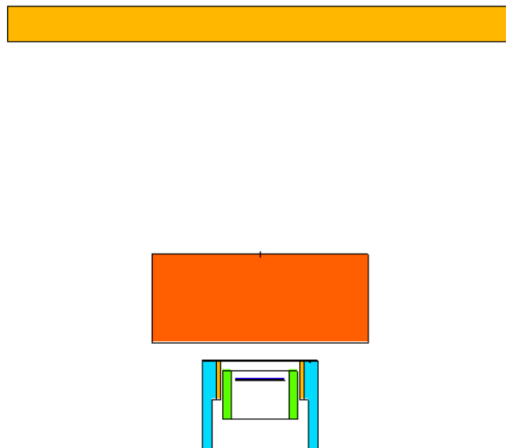
Figure 4.3: Simulation geometry of the IVXRF system for a soft tissue target 0.5 cm away from the system. The target (orange) is 0.5 cm away from the front of the system, the lead shielding behind the target during experiments is shown (yellow), and the SDD & cap is also shown.
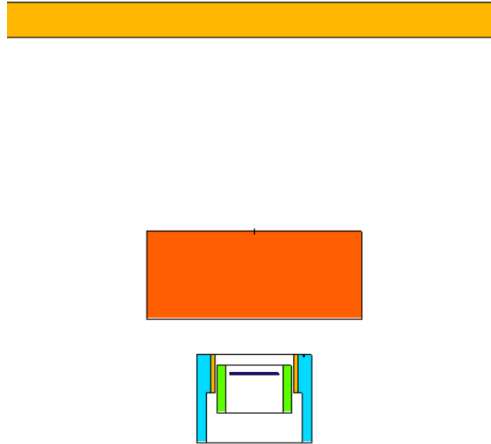
Figure 4.4: Simulation geometry of the IVXRF system for a tissue target 1 cm away from the system.
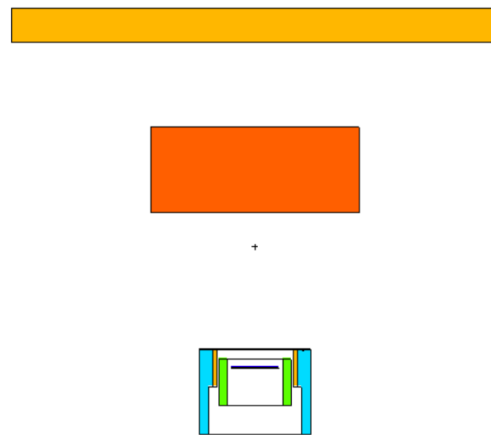

Figure 4.5: Simulation geometry of the IVXRF system for a tissue target 4 cm away from the system.

The depth distribution simulations also used an ICRU-defined four-component soft tissue-equivalent material to comprise the target. The target also included a 1 mm thick layer of iron that was placed

at different depths, ranging from on the surface of the sample (d = 0 mm) to 3 mm within the sample (d = 3 mm) at intervals of 0.2 mm. Figures 4.6 and 4.7 show the geometry of the depth distribution simulations.
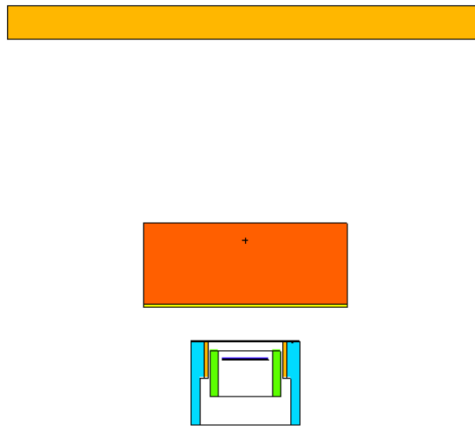

Figure 4.6: Simulation geometry of the IVXRF system for a water target (blue) 1 cm away from the system and 1 mm iron layer (orange) on the target's surface (depth = 0 mm).
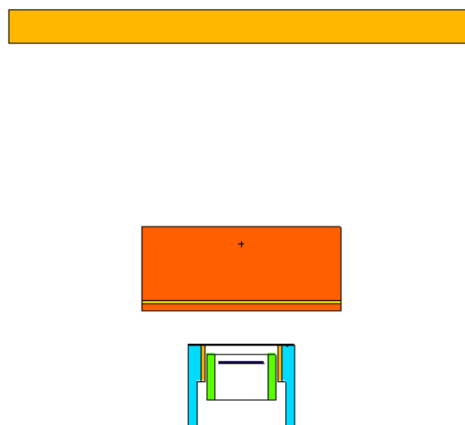

Figure 4.7: Simulation geometry of the IVXRF system for a water target 1 cm away from the system and 1 mm iron layer 2 mm deep into the target.

4.3   Simulation spectra

To determine the iron counts detected from the target for different depths of iron accumulation, spectral analysis was conducted on the depth distribution simulations for varying depths of the 1 mm iron layer. The spectra were collected using an F4 tally on the active volume of the SDD to determine the average flux of particles onto the active volume. The iron kα peak was analyzed to determine the counts of iron x-rays.

Note the delta-like behaviour of the iron peaks within the spectra compared to the Gaussian curve-like behaviour of the peaks within the experimental spectra. Within the experimental spectra, there are many factors that lead to the formation of Gaussian peaks. [18] Statistical variation in the charge carriers of the SDD, from the number of charge carriers to the loss of energy from the dead layer, contributes to the formation of Gaussian-like variance. Other factors also contribute to spectral broadening, such as electronic noise affecting pulse processing. These factors that contribute to spectral broadening were not included in the simulations. As a result, the peaks in the simulated spectra are more delta-like in behaviour than those of the experimental spectra.
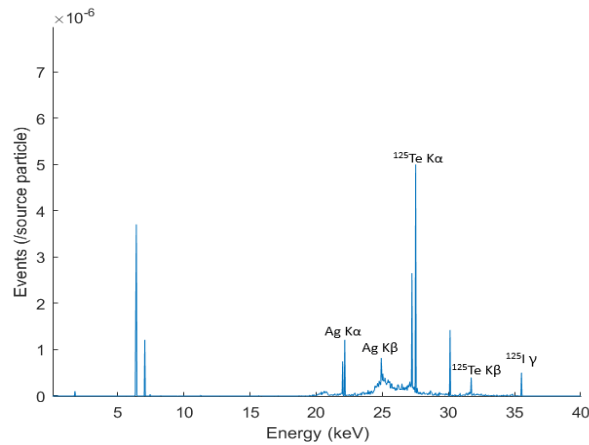

Figure 4.8: Simulated spectrum of a soft tissue target with a 1 mm iron layer on the target surface.
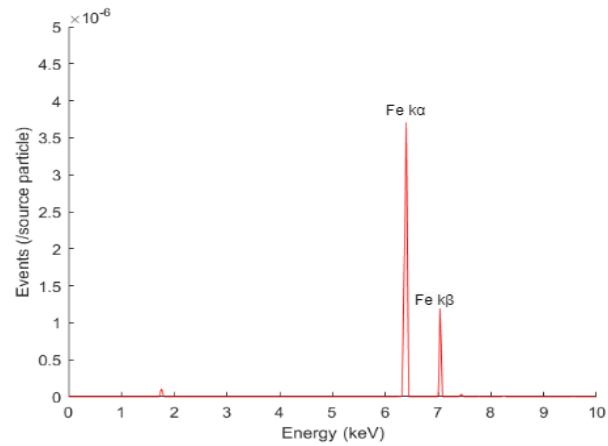
Figure 4.9: Simulated spectrum of a soft tissue target with a 1 mm iron layer on the target surface
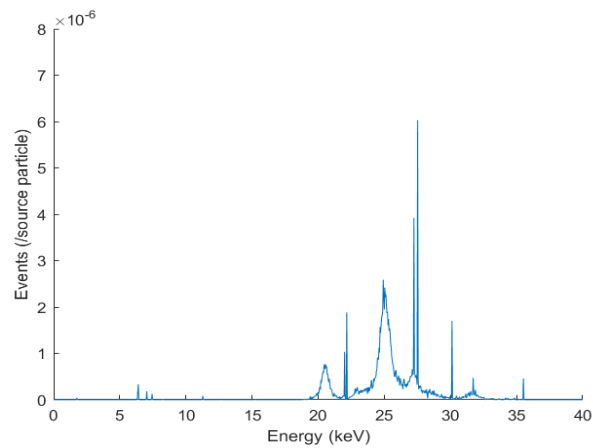
in the energy range of 0 to 10 keV.

Figure 4.10: Simulated spectrum of a soft tissue target with a 1 mm iron layer at a depth of 1 mm
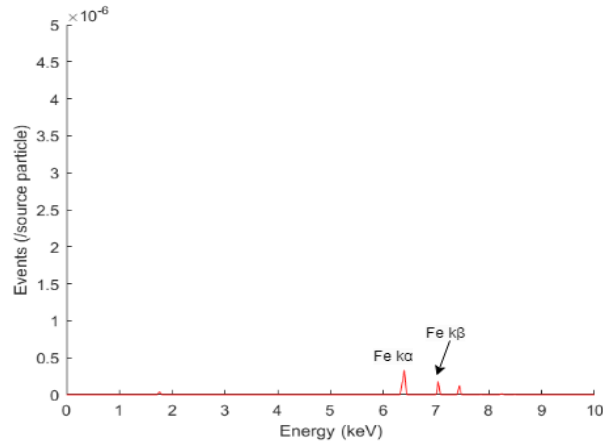
within the target.

Figure 4.11: Simulated spectrum of a soft tissue target with a 1 mm iron layer at a depth of 1 mm within the target in the energy range of 0 to 10 keV.

Figures 4.8 and 4.9 show the spectrum of the soft tissue target with the iron layer at its surface. This spectrum presents strong kα and kβ peaks, as iron fluorescence x-rays heading towards the detector would not undergo attenuation from the soft tissue target.

Figures 4.10 and 4.11 shows the spectrum of the soft tissue target with an iron layer at a depth of 1 mm within the target. Like figures 4.8 and 4.9, the iron kα and kβ peaks are present; however, they are less prominent. This is due to how the fluorescence x-rays heading towards the detector will be attenuated by the soft tissue target itself.

4.4 Dosimetry

The dosimetry simulations simulated a soft tissue target in exposure to the system for measurement. The F6 tally of MCNP was used to determine the energy deposition onto the target. Figure 4.12 shows a sample spectrum collected using an F4 tally on the active volume.

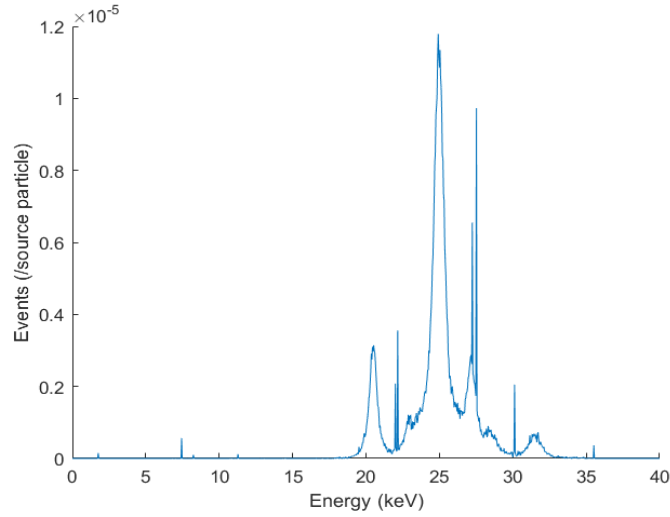Figure 4.12: Simulated spectrum of a soft tissue target 1 cm away from the system.

To account for the effects of different radiation types and organs on dose, the effective dose, E, of the system was calculated. This can be calculated with the following equation:

$$E = \Sigma_{n=1}^{i} D w_r w_{t,i} \frac{volume_{irradiated,i}/d}{surface_{total,i}} \tag{3}$$

Where D is the simulated absorbed dose of the target, w_r is the radiation weighting factor, w_i is the organ weighting factor of the particular organ, volume$_{irradiated,i}$ is the irradiated volume of the target, d is the average depth of penetration of incident radiation, and surface$_{total,i}$ is the total surface area of a particular organ. The skin's total surface area was taken to be equal to that of a reference man, as taken from ICRP 89. [37] For this calculation, only the dose to skin was considered, and as such, the contribution to effective dose from other organs was not considered.

The equivalent dose of the system, H, is the radiation-weighted dose of a target averaged over an entire organ. From ICRP 60, the radiation weighting factor of all the photons from the source is 1: as such, w_r was taken to be 1. Once the radiation weighting factor was determined, the effective dose,

E, of the system can then be calculated. Assuming that only skin was exposed, the organ weighting factor of skin can be taken, which Table 4.1 shows to be 0.01. Given that the target volume is 22.5π cm^3 (about 70.7 cm^3), the total surface area of a reference man is 1.9 m^2, and the average penetration depth of incident radiation is equal to the depth of the target (2.5 cm), the effective dose can be calculated. It should be noted that a depth of 2.5 cm was used as it matched the average mean free path of the source particles (approximately 2.4 cm), and as such, is a conservative estimate.

Organ	Weighting factor	Sum of weighting factors
Gonads	0.20	0.20
Red marrow, colon, lung, stomach	0.12	0.48
Bladder, breast, liver, esophagus, thyroid, remainder	0.05	0.30
Skin, bone surface	0.01	0.02

Table 4.1: Table of tissue weighting factors as cited in ICRP 119. [38]

It should be noted that the simulation only accounted for the radiation dose arising from the system onto the target, and does not factor in the potential dose that could arise due to incident radiation on other parts of the body. More extensive simulations should be conducted to understand the effective dose and subsequent health risk of the system.

4.5   Conclusion

In this section, details of the Monte Carlo simulations not discussed in the paper were discussed. This chapter is intended to be read as an adjunct to the submitted article to provide further context on the simulation work that was performed.

Chapter 5

5   Conclusion

The ^{125}I-based x-ray fluorescence system was feasible in measuring *in vivo* skin iron levels, as it has been shown to result in a low dose and minimum detection limit within a reasonable measurement time of 1800 s real-time. With that, there are many avenues for the work of this study to be expanded upon that will contribute to the goal of the clinical implementation of the system.

Limitations and potential future work of this system have been previously discussed in the Limitations section of Chapter 2. This Chapter will therefore expand on the material introduced within that section, providing further context.

5.1   X-ray Fluorescence System Characterization

While the ^{125}I-based IVXRF system has an MDL that allows it to be theoretically capable of measuring the blood iron levels of normal and iron-overloaded patients, it does not have a low MDL compared to other IVXRF systems for the measurement of iron that employ ^{109}Cd as the fluorescing source. [39] The system could potentially be improved in a few ways to enhance its applicability. Most notably, the source used in the study was collimated only by the aluminum cap and does not employ additional collimation. Including an additional collimator would have many benefits for the system, as it allows for a more focused beam of radiation incident on the target. These potential benefits would include lowering the minimum detectable limit and reducing the potential dose of individuals in the surrounding area.

Adding a collimator can potentially increase the system's MDL. A previous study exploring the effects of collimation on an IVXRF system that measures bone cadmium found that the diameter of a collimator affects its MDL. [40] Photons at large angles can be absorbed or scattered toward the

target, resulting in a more focused beam. It should be noted that the change in MDL varied based on the detector system used and that an SDD was not explored in the study. As a result, work will need to be done to compare the effect of different collimation diameters with an SDD.

The length of the collimator should be considered when optimizing the system. A previous study exploring collimator lengths in a K-XRF system to measure bone cadmium levels found that longer collimator lengths lead to a higher MDL. [41] As such, this length should be optimized.

Collimation will also allow the system to reduce its dose to surrounding individuals. With a less focused beam, the system risks excessively irradiating individuals in its vicinity. Focusing the beam onto the target will help in reducing such exposure.

Another possible avenue for improving the system is increasing the source strength. Due to the low effective dose from the IVXRF system, a stronger source can be employed to improve the system while also ensuring the potential risk of the system is minimal.

Finally, the pulse processing chain of the detector can be modified to allow for enhanced signal processing. One of the limiting variables that come with radiation detectors is the associated rise time that comes with incoming pulses. This rise time can also affect the processing and detection of different particles, which can lead to particles being missed by the system. Modifying the pulse processing chain of the system can ensure that increasing the activity of the source will have minimal effect on the system dead time. For example, the rise time of the system was set at 1 μs - adjusting the pulse shaper of the system to allow for a shorter rise time can allow for more particles to be detected and processed.

5.2   *Ex vivo* rat skin study

The study was run under the assumption that the Huber x-ray fluorescence system is a benchmark of skin iron concentration measurement, as it allows for a more controlled environment during measure-

ments than the IVXRF system. However, other measurement methods can be employed to compare to the IVXRF system. Future studies comparing the XRF system to other forms of elemental analysis, like inductively coupled plasma mass spectrometry (ICP-MS), will aid in further verifying the accuracy of the system in measuring skin iron. [42]

In addition, comparative studies of rat skin sample measurements to other rat organ sample measurements using the IVXRF system can be conducted. Previous studies comparing rat skin measurements measured with a handheld XRF system and rat organ measurements have been done by Dao et al. [43] These studies can help further validate that the IVXRF system can effectively measure the iron load of different organs by correlating the measured iron load of organs like the liver and heart with skin iron measurements.

5.3   Monte Carlo Simulations

Dosimetry measurements were performed exclusively using Monte Carlo simulations, and they did not include measurements with dosimetry instruments such as dosimetry chips or dosimeters. This limited investigation of dosimetry was due to supplier delays in providing dosimetry chips. Comparing measurements read on dosimetry chips with the simulation results will validate the simulation's calculation of the expected dose from this IVXRF system.

One of the assumptions made with calculating dose is that only the dose to skin was considered and that the dose to other organs of the body was not considered. Further work to validate the simulations can also include adding additional elements to the simulations. For example, simulating the typical geometry of a patient undergoing a measurement can help determine a more holistic view of their effective whole-body dose. In addition, simulations can also be run with more irregularly-shaped targets to quantify how measurements can be affected.

5.4   Conclusion

As discussed previously, the ^{125}I-based IVXRF system, study design, and simulations can be explored in many different ways to develop the IVXRF system. Nevertheless, the system has been shown to be theoretically capable of accurately measuring skin iron levels in normal and iron-overloaded patients. It also results in a low effective dose, lower than those delivered in current medical diagnostic procedures. This study lays the groundwork to develop the ^{125}I-based IVXRF system into a cost-efficient, non-invasive, and accurate clinical tool to help physicians treat iron-overloaded patients.

Works Cited

References

[1] Renzo Galanello and Raffaella Origa. "Beta-thalassemia". In: *Orphanet journal of rare diseases* 5 (2010), pp. 1–15.

[2] Robert E Fleming and Prem Ponka. "Iron overload in human disease". In: *New England Journal of Medicine* 366.4 (2012), pp. 348–359.

[3] Antonello Pietrangelo. "Hereditary hemochromatosis—a new look at an old disease". In: *New England Journal of Medicine* 350.23 (2004), pp. 2383–2397.

[4] Hiroshi Kawabata. "Transferrin and transferrin receptors update". In: *Free Radical Biology and Medicine* 133 (2019), pp. 46–54.

[5] Dimitrios T Kremastinos et al. "β-thalassemia cardiomyopathy: history, present considerations, and future perspectives". In: *Circulation: Heart Failure* 3.3 (2010), pp. 451–458.

[6] Antonello Pietrangelo. "Hereditary hemochromatosis: pathogenesis, diagnosis, and treatment". In: *Gastroenterology* 139.2 (2010), pp. 393–408.

[7] Colm J Murphy and Gavin Y Oudit. "Iron-overload cardiomyopathy: pathophysiology, diagnosis, and treatment". In: *Journal of cardiac failure* 16.11 (2010), pp. 888–900.

[8] Raffaella Origa. "β-Thalassemia". In: *Genetics in Medicine* 19.6 (2017), pp. 609–619.

[9] Yesim Aydinok. "Thalassemia". In: *Hematology* 17.sup1 (2012), s28–s31.

[10] Neeraj Shah et al. "Study on effectiveness of transfusion program in thalassemia major patients receiving multiple blood transfusions at a transfusion centre in Western India". In: *Asian journal of transfusion science* 4.2 (2010), p. 94.

[11]   Brian K Crownover and Carlton Covey. "Hereditary hemochromatosis". In: *American family physician* 87.3 (2013), pp. 183–190.

[12]   Nancy F Olivieri and Gary M Brittenham. "Iron-chelating therapy and the treatment of thalassemia". In: *Blood, The Journal of the American Society of Hematology* 89.3 (1997), pp. 739–761.

[13]   Caterina Borgna-Pignatti and Maria Marsella. "Iron chelation in thalassemia major". In: *Clinical therapeutics* 37.12 (2015), pp. 2866–2877.

[14]   John C Wood. "Use of magnetic resonance imaging to monitor iron overload". In: *Hematology/Oncology Clinics* 28.4 (2014), pp. 747–764.

[15]   Diego Hernando et al. "Quantification of liver iron with MRI: state of the art and remaining challenges". In: *Journal of Magnetic Resonance Imaging* 40.5 (2014), pp. 1003–1021.

[16]   Axel Dignass, Karima Farrag, Jürgen Stein, et al. "Limitations of serum ferritin in diagnosing iron deficiency in inflammatory conditions". In: *International journal of chronic diseases* 2018 (2018).

[17]   Burkhard Beckhoff et al. *Handbook of practical X-ray fluorescence analysis*. Springer Science & Business Media, 2007.

[18]   Glenn F Knoll. *Radiation detection and measurement*. John Wiley & Sons, 2010.

[19]   Albert C. Thompson. *X-ray data booklet*. Lawrence Berkeley National Laboratory, University of California, 2009.

[20]   DR Chettle. "Three decades of in vivo x-ray fluorescence of lead in bone". In: *X-Ray Spectrometry: An International Journal* 34.5 (2005), pp. 446–450.

[21]   Lars Ahlgren et al. "X-ray fluorescence analysis of lead in human skeleton in vivo". In: *Scandinavian journal of work, environment & health* (1976), pp. 82–86.

[22] Lillian J Somervaille, David R Chettle, and Malcolm C Scott. "In vivo measurement of lead in bone using x-ray fluorescence". In: *Physics in Medicine & Biology* 30.9 (1985), p. 929.

[23] Howard Hu, Antonio Aro, and Andrea Rotnitzky. "Bone lead measured by X-ray fluorescence: epidemiologic methods." In: *Environmental Health Perspectives* 103.suppl 1 (1995), pp. 105–110.

[24] A Pejović-Milić et al. "Quantification of bone strontium levels in humans by in vivo x-ray fluorescence". In: *Medical physics* 31.3 (2004), pp. 528–538.

[25] Helen Moise, David R Chettle, and Ana Pejović-Milić. "Monitoring bone strontium intake in osteoporotic females self-supplementing with strontium citrate with a novel in-vivo X-ray fluorescence based diagnostic tool". In: *Bone* 61 (2014), pp. 48–54.

[26] Andrew P Bagshaw and Michael J Farquharson. "Simultaneous determination of iron, copper and zinc concentrations in skin phantoms using XRF spectrometry". In: *X-Ray Spectrometry: An International Journal* 31.1 (2002), pp. 47–52.

[27] Marcelo Estevam and Carlos Roberto Appoloni. "Use of portable x-ray fluorescence (PXRF) in vivo as an alternative technique for the assessment of iron levels in patients with thalassemia and hemochromatosis". In: *Health physics* 104.2 (2013), pp. 132–138.

[28] Pedro Andreo. "Monte Carlo techniques in medical radiation physics". In: *Physics in Medicine & Biology* 36.7 (1991), p. 861.

[29] H-P Chan and Kunio Doi. "The validity of Monte Carlo simulation in studies of scattered radiation in diagnostic radiology". In: *Physics in Medicine & Biology* 28.2 (1983), p. 109.

[30] David Sarrut et al. "A review of the use and potential of the GATE Monte Carlo simulation code for radiation therapy and dosimetry applications". In: *Medical physics* 41.6Part1 (2014), p. 064301.

[31] M Zamburlini et al. "In vivo study of an x-ray fluorescence system to detect bone strontium non-invasively". In: *Physics in Medicine & Biology* 52.8 (2007), p. 2107.

[32] Ryan CN Studinski et al. "Estimation of a method detection limit for an in vivo XRF arsenic detection system". In: *Physics in Medicine & Biology* 50.3 (2005), p. 521.

[33] John H Hubbell. "Tables of x-ray mass attenuation coefficients and mass energy-absorption coefficients". In: *http://physics. nist. gov/PhysRefData/XrayMassCoef/* (1996).

[34] Mark J Rivard et al. "Supplement to the 2004 update of the AAPM Task Group No. 43 Report". In: *Medical physics* 34.6Part1 (2007), pp. 2187–2205.

[35] Mark J Rivard et al. "Update of AAPM Task Group No. 43 Report: A revised AAPM protocol for brachytherapy dose calculations". In: *Medical physics* 31.3 (2004), pp. 633–674.

[36] ICRU. "Tissue substitutes in radiation dosimetry and measurement. no. 4". In: *Radiology* 173.1 (1989), pp. 202–202.

[37] ICRP. "Basic anatomical and physiological data for use in radiological protection: reference values: ICRP Publication 89: Approved by the Commission in September 2001". In: *Annals of the ICRP* 32.3-4 (2002), pp. 1–277.

[38] IRCP. "ICRP publication 119: compendium of dose coefficients based on ICRP publication 60". In: *Annals of the ICRP* 41 (2012), pp. 1–130.

[39] Sami Ullah Khan Bangash et al. "Feasibility of a 109Cd-based portable XRF device for measuring skin iron concentration in anaemic and β- Thalassaemic patients". In: *Biomedical Physics & Engineering Express* 8.6 (2022), p. 065034.

[40] M Popovic et al. "Improvement in the detection limit of anin vivo XRF cadmium detection system". In: *Journal of radioanalytical and nuclear chemistry* 269 (2006), pp. 421–424.

[41] SE Carew et al. "Development of a K-shell x-ray fluorescence measurement of cadmium in bone". In: *X-Ray Spectrometry: An International Journal* 34.6 (2005), pp. 498–501.

[42] Renata S Amais, George L Donati, and Marco A Zezzi Arruda. "ICP-MS and trace element analysis as tools for better understanding medical conditions". In: *TrAC Trends in Analytical Chemistry* 133 (2020), p. 116094.

[43] E Dao et al. "Feasibility of the use of a handheld XRF analyzer to measure skin iron to monitor iron levels in critical organs". In: *Journal of Trace Elements in Medicine and Biology* 50 (2018), pp. 305–311.